Zipping-Depinning: Dissolution of Droplets on Micropatterned Concentric Rings

José Encarnación Escobar, Erik Dietrich, S. Arscott, Harold J. W. Zandvliet, Xuehua Zhang, Detlef Lohse

LANGMUIR Article
Cite This: Langmuir 2018, 34, 5396−5402
pubs.acs.org/Langmuir

Zipping-Depinning: Dissolution of Droplets on Micropatterned Concentric Rings

José M. Encarnación Escobar,*[,†] Erik Dietrich,[‡] Steve Arscott,[§] Harold J. W. Zandvliet,[‡] Xuehua Zhang,*[,∥] and Detlef Lohse*[,†,⊥]

[†]Department of Physics of Fluids and [‡]Department of Physics of Interfaces and Nanomaterials, University of Twente, P.O. Box 217, 7500AE Enschede, The Netherlands

[§]Institut d'Electronique, de Microélectronique et de Nanotechnologie, CNRS, The University of Lille, Villeneuve d'Ascq 59652, France

[∥]Department of Chemical & Materials Engineering, University of Alberta, Edmonton, Alberta T6G 2R3, Canada

[⊥]Max Planck Institute for Dynamics and Self-Organization, 37077 Goettingen, Germany

ABSTRACT: The control of the surface wettability is of great interest for technological applications as well as for the fundamental understanding of surface phenomena. In this article, we describe the dissolution behavior of droplets wetting a micropatterned surface consisting of smooth concentric circular grooves. In the experiments, a droplet of alcohol (1-pentanol) is placed onto water-immersed micropatterns. When the drops dissolve, the dynamics of the receding contact line occurs in two different modes. In addition to the stick-jump mode with jumps from one ring to the next inner one, our study reveals a second dissolution mode, which we refer to as zipping-depinning. The velocity of the zipping-depinning fronts is governed by the dissolution rate. At the early stage of the droplet dissolution, our experimental results are in good agreement with the theoretical predictions by Debuisson et al. [*Appl. Phys. Lett.* **2011**, *99*, 184101]. With an extended model, we can accurately describe the dissolution dynamics in both stick-jump and zipping-depinning modes.

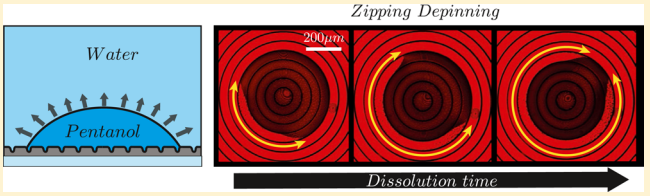

INTRODUCTION

Wetting on structured surfaces is of great importance in many natural, technological, and industrial processes. This holds for the control of droplets for self-cleaning,[2,3] antifogging,[4] anticing,[5] water harvesting,[6] phase change heat transfer,[7−9] evaporative self-assembly of nanomaterials,[10−13] manipulation of micro- and nanosized objects,[14] construction of circuits,[15−18] or droplet-based analysis and diagnostics,[19] among many others. Correspondingly, significant advances have been achieved in the fundamental understanding of drop dynamics on a variety of microstructures.[20−28] Several modes of drop evaporation have been observed, including constant contact angle, constant contact radius, stick-slide mode, and stick-jump mode.[29−32] Pinning at the contact line of the drop, the surrounding fluid phase, and properties of the substrate are all essential to control the evaporation and dissolution modes and transitions between them.[33−38] Chemical or geometrical surface features even down to sub-nanometer scale may give rise to pinning effects, imparting the lifetime of the evaporating or dissolving sessile drops.[39,40]

The mechanical stability and lifetime of drops may be potentially tuned by well-defined surface structures. Among a variety of surface microstructures, engraved concentric microrings may pin the entire three-phase boundary of a drop, representing an interesting case of an extremely strong pinning effect. It was reported that microring structures are the most effective in stabilizing droplets against mechanical and chemical perturbations, compared with other microtopographical features of trenches or plateaus.[19] Such stability of drops is highly desirable, e.g., for the hanging drop technique for long-term cell cultures[19] and other techniques for analytical and clinical diagnostic screening.[41]

To understand the dynamics of drops on the substrate patterned with concentric microrings, Kalinin et al.[42] measured critical apparent advancing and receding angles and correlated them with the morphological characteristics of the rings. They found that the apparent critical angles were independent of the ring height and width, but were determined primarily by the slope of the ring sidewalls.[42] Debuisson et al. quantitatively showed that concentric microrings facilitate the stick-jump model of evaporating drops. They also found that for a given droplet radius, the smaller the spacing of the rings, the shorter the evaporation time. It was shown that the contact line depins when the liquid micromeniscus simultaneously touches both sides of the groove (Figure 2). Assuming volume conservation during jumping of the contact line to the next ring, a model was developed to explain the contact angle hysteresis.[1] Debuisson et al. also showed that the contact angle hysteresis and the

Received: January 24, 2018
Revised: March 19, 2018
Published: April 13, 2018

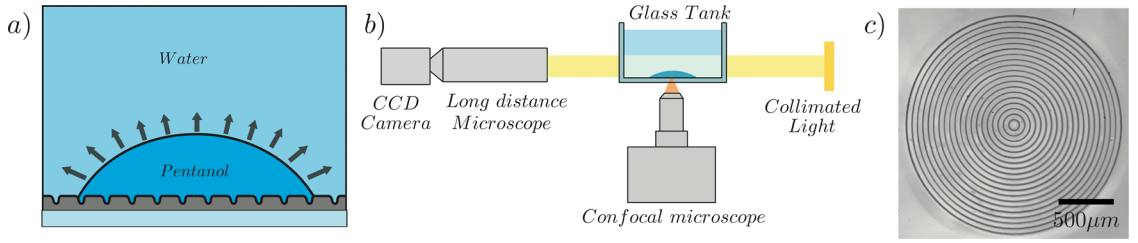

Figure 1. (a) Schematic diagram of a dissolving drop on microrings in the experiments. (b) Setup to observe the dissolution process. The dissolving alcohol droplet immersed in water was imaged from side and bottom to extract data about both the contact diameter and contact angle. (c) Bottom view of microring patterns with a spacing of 50 μm.

evaporation behavior of the drop can be further modified by introducing a gap as an artificial defect on the ring.[44]

In this work, we focus on the depinning behavior of droplets from the microrings during the dissolution in a partially miscible liquid surrounding phase. We extracted the contact angles as a function of time from the experimental data and compared them with the predictions by Debuisson et al.[1] We found that this model works well for the case when the transitions from ring to ring occur on a time scale much shorter than the corresponding shrinkage of the droplet. However, when the time scales become comparable, our results reveal another mode of zipping-depinning (ZD). As far as we know, this new mode has not been reported in the literature yet. We theoretically analyze this zipping-depinning mode and can quantitatively describe the overall dissolution.

EXPERIMENTAL SECTION

Thin glass substrates with thickness of 170 μm were used as the substrate, which are optimal for confocal microscopic imaging. The fabrication of the micropatterned surfaces was done using a standard photolithography process on the thin glass slides. The concentric rings are at a distance of 50 μm from each other. The detailed protocol was reported in a previous work.[43]

The experiments were conducted in a transparent container with dimensions 5 × 5 × 5 cm^3, as sketched in Figure 1a,b, next to an image of one of the substrates used (Figure 1c). Before each experiment, the tank was cleaned thoroughly using isopropylalcohol (Sigma-Aldrich) and water. The container was first filled with purified water (Merck Milipore, 18.2 MΩ cm), and then the substrate was immersed in the water. A droplet of 1-pentanol was carefully placed on the center of the concentric rings on the surface by using a glass syringe with a long aluminum needle with a diameter of 210 μm. The dispensing rate of the drop was controlled by a syringe pump.

In all experiments, the images of the drop were recorded from a side and bottom view. The side view of the drop was taken under illumination of a collimated light with a CCD camera through a long working distance microscope lens, from which the contact angles and height of the drops were extracted. The bottom view was taken with a confocal microscope (Nikon A1+) in a transmission mode. In the measurements, we monitor the shape of the droplet on the solid surface and the contact line of the droplet during the dissolution process.

EXPERIMENTAL RESULTS

Pinning and Depinning Condition. The definitions of all of the parameters and notations in this work are shown in Figure 2. θ is the real contact angle, measured with respect to the tangent of the substrate and $\overline{\theta}$ is the apparent contact angle measured with respect to the flat substrate. θ_r stands for the receding contact angle and θ^* for the contact angle at the depinning condition, which is also the apparent contact angle at the depinning condition. The drop is of 1-pentanol, and the surrounding phase is water.

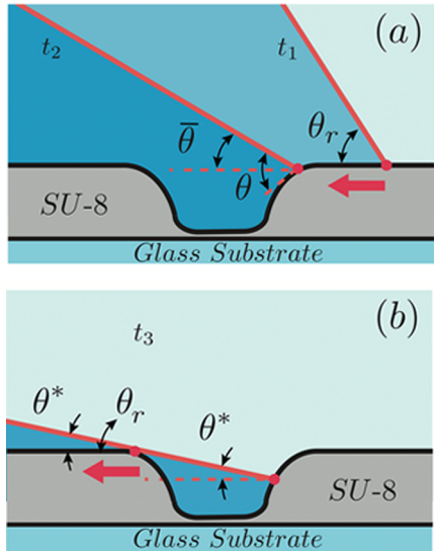

Figure 2. Illustration of the movement of the contact line across a smooth defect. The drop shrinks toward the center on the left. Dark blue represents the bulk of the alcohol droplet, whereas light blue represents the bulk of the water in which the drop is immersed (a) receding contact line (at a time t_1) and pinned contact line (at a time t_2). (b) Condition for depinning (at a time t_3), where θ is the real contact angle, measured with respect to the tangent of the substrate, $\overline{\theta}$ is the apparent contact angle measured with respect to the flat substrate, the subindex "r" stands for receding, and the super index "*" indicates the depinning condition. θ^* is the contact angle at the new contact line.

In the early stages, the drop dissolves in a stick-jump mode (see Figure 3). The jumps are triggered by the geometrical depinning condition as shown in Figure 2. When the contact line encounters a defect, a transition to the constant contact radius mode is observed. The drop will shrink by decreasing simultaneously the height and contact angle, while its footprint area remains constant (Figure 2a). As the drop dissolves, the actual contact angle θ is larger than the receding angle, θ_r, as shown in Figure 2a ($\theta > \theta_r$). We note that the relative contact angle is measured with respect to the flat part of the substrate, i.e., the groove-free surface. As the contact angle reaches a critical value, i.e., the depinning contact angle θ^*, the surface of the drop touches the other side of the groove (Figure 2b), creating a new contact line with a new effective contact angle θ^*. The new contact angle θ^* is much smaller than the receding contact angle at that point ($\theta^* \ll \theta_r$), causing the detachment of the contact line from the ring. The full contact line depins from the ring "at once" (jump phase of the stick-jump mode), i.e., we cannot temporally resolve any spatial variation of the jump in azimuthal direction. In this case, the contact line moves uniformly in the radial direction until it encounters a new groove and becomes pinned again (see Figure 2a). The main features of each phase in the stick-jump mode are consistent with the depinning process of evaporative drops on the ring micropatterns.[1,43]

DOI: 10.1021/acs.langmuir.8b00256
Langmuir 2018, 34, 5396−5402

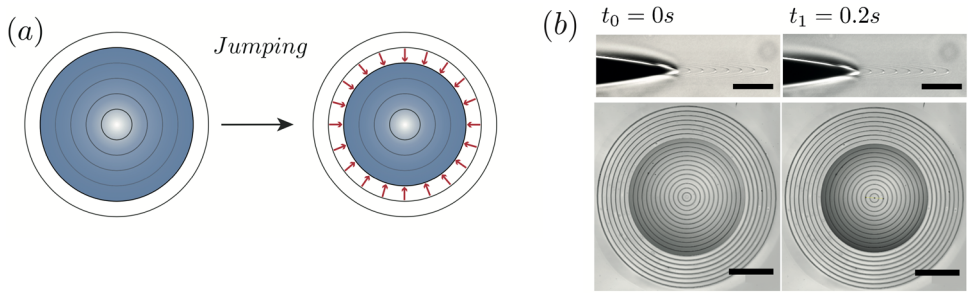

Figure 3. Stick-jump mode. (a) Sketch of the stick-jump model. (b) Experimental side and bottom view images of the drop in the stick-jump mode (synchronized). Scale bar in side view images: 150 μm. The distance between rings is 50 μm. Scale bar in bottom view images: 500 μm.

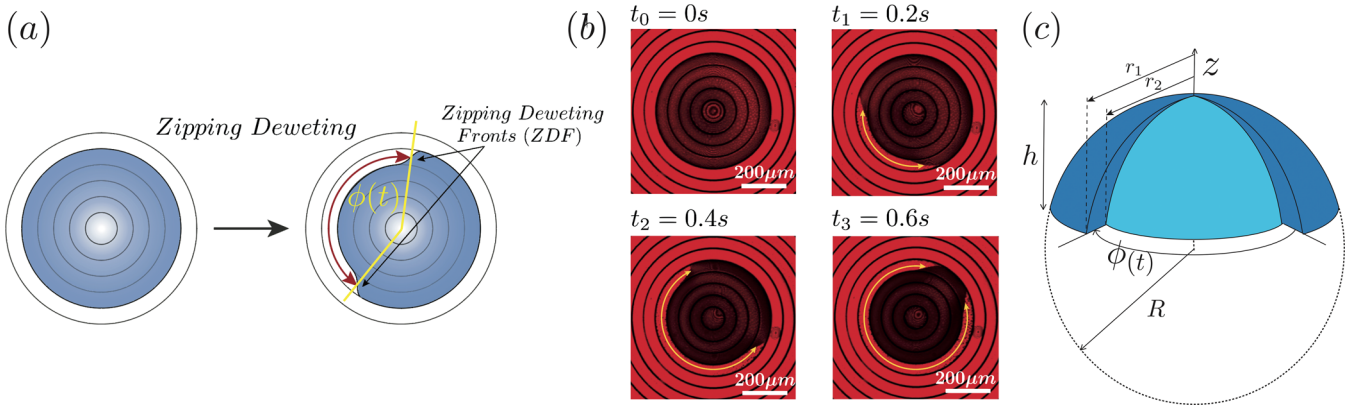

Figure 4. Zipping-depinning model. (a) Scheme of zipping-depinning mode. (b) Snapshots of consecutive experimental pictures of the drop at four different times, revealing the zipping-depinning behavior with the azimuthal angle $\phi(t)$ between the ZDFs growing. (c) Illustration of the geometric model as two portions of spherical caps having the same the apex but different radii. As the ZDFs advance, the angle $\phi(t)$ increases with a rate $\omega(t) = d\phi/dt$.

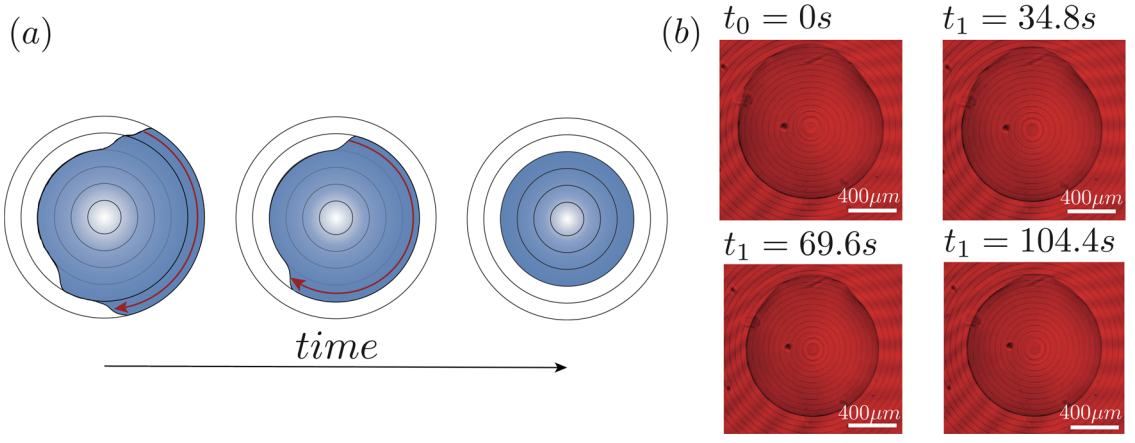

Figure 5. (a) Illustration of the self-centering process. The mass loss from the drop leads to zipping-depinning and hence to self-centering of the drop. The red arrows show the typical azimuthal movement of the zipping-depinning fronts during the self-centering process. (b) Experimental example of the self-centering process shown in four bottom view frames taken at intervals of 34.8 s.

Zipping-Depinning Mode and Self-Centering. At the late stage of drop dissolution, we observed the new zipping-depinning (ZD) mode. An example is shown in Figure 4. This mode is the result of the movement of the contact line constrained by the concentric rings. During this movement, part of the contact line remains pinned to the ring, while a section of the contact line has already moved and pinned to the following ring. This creates two fronts of the contact line between both rings (see Figure 4a). These fronts recede in the azimuthal direction, following the rings, until the entire contact line detaches from the outer ring. We refer to these fronts as zipping-depinning fronts (ZDFs). At t = 0 s, the contact line is fully in contact with an outer ring. At t = 0.2 s, the snapshots clearly show that only a part of the contact line depins and pins at the following ring, whereas the rest of the contact line remains pinned at the outer ring. These fronts recede along the rings, and a larger portion of the contact line zipped off at t = 0.4 and 0.6 s. Eventually, the two fronts meet each other and the entire contact line detaches from the outer ring. We refer to this mode as the zipping-depinning (ZD) mode and these fronts as zipping-depinning fronts (ZDFs) (see Figure 4).

In practice, the drop is not always perfectly centered (imperfect centering of the needle and wetting of the substrate). The off-centered drop unzips more than one ring at the same time. This scenario is sketched in Figure 5a next to an experimental example (b), where the receding fronts of the unzipping contact line recede between two

DOI: 10.1021/acs.langmuir.8b00256
Langmuir 2018, 34, 5396−5402

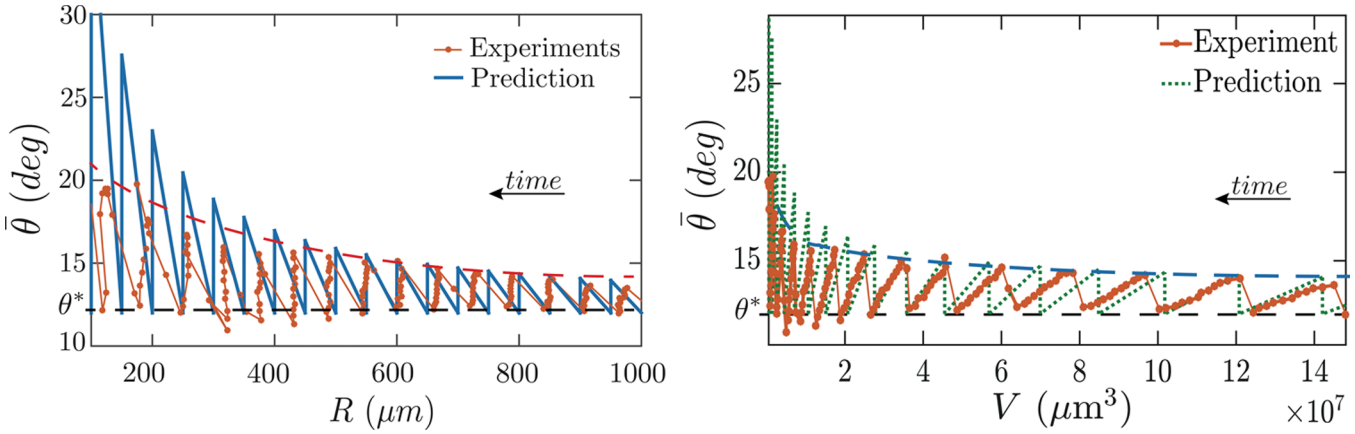

Figure 6. Experimental data of the variation of the contact angle during the dissolution of a drop on smooth concentric rings separated 50 μm versus the radius R and versus the volume V, respectively. We also show the prediction based on the conservation of volume during the jump, as proposed by Debuisson et al.[1] (eq 2). The experimental data and theoretical prediction agree well at the early stage of the droplet dissolution, but not at later stages. The red and black dotted lines in the graphs are only guidelines to the eye and show, respectively, the mismatch at later stages of dissolution and the constant apparent depinning angle θ^*.

adjacent rings. In this process, the mass loss during the dissolution of the drop leads to a slow (as compared with the stick-jump mode) sequence of zipping-depinning-like movements along the bigger diameter rings until the droplet self-centers; see Figure 5b. We refer to this process as a self-centering process. The size of the droplets is large compared with the spacing between the rings and the size of the grooves. So, in this case, the relative change in volume associated with the movement of the zipping-depinning fronts is relatively small. Moreover, the contact angle is larger than that observed before depinning, implying smaller dissolution rates.[45] The movement of the contact line is much slower than that—as we shall see below—observed in the case of the zipping-depinning during the later stages of the dissolution process; see Figure 5b.

THEORETICAL ANALYSIS OF ZIPPING-DEPINNING MODE

The contact angle $\bar{\theta}$ during the entire dissolution process is plotted as a function of time in Figure 6. The apparent depinning contact angle θ^* before each depinning was constant at the value of ≈12°. Using this apparent depinning contact angle of $\theta^* \approx 12°$, we calculate the angles $\bar{\theta}_2$. Here, $\bar{\theta}_2$ is the angle of the drop immediately after the jump.

We assume that the jumps are instantaneous and that the drop volume during the jump is conserved. The drop volume immediately before the depinning is then given by

$$V_1(\theta^*, r_1) = \frac{\pi r_1^3}{3\theta^*} \sin\theta^* \frac{2 + \cos\theta^*}{(1 + \cos\theta^*)^2} \quad (1)$$

where r_1 is the radius of the patterned ring and θ^* is the depinning contact angle. Using the same expression, we can calculate the contact angle $\bar{\theta}_2$ corresponding to a droplet with the same volume but with a radius r_2. Here, the indices 1 and 2 correspond to the rings before and after the jump, respectively. From volume conservation $V_1(\theta^*, r_1) = V_2(\bar{\theta}_2, r_2)$, we obtain

$$\frac{\pi r_1^3}{3\theta^*} \sin\theta^* \frac{2 + \cos\theta^*}{(1 + \cos\theta^*)^2} = \frac{\pi r_2^3}{3\bar{\theta}_2} \sin\bar{\theta}_2 \frac{2 + \cos\bar{\theta}_2}{(1 + \cos\bar{\theta}_2)^2} \quad (2)$$

The predicted contact angles are plotted together with experimental data in Figure 6, showing good agreement for $\bar{\theta}_2$ at the early stages up to the drop radius of $R \approx 500$ μm. However, in the later stage of the dissolution process, $\bar{\theta}_2$ turns out to be significantly smaller than the predictions. The transition from ring to ring in the experiments takes more time than the theoretical prediction. This significant discrepancy suggests that the stick-jump mode is not accurate enough to account for the entire dissolution process. Below, we will develop a modified model to properly represent the dissolution during the stick-jump and the zipping-depinning modes.

For the prediction of the contact angle $\bar{\theta}_2$, it is important to properly understand the movement of the contact line during the depinning−pinning transition. The duration of the zipping-depinning was found experimentally to vary from one ring to another. We determine the average angular velocity $\omega = d_c/t_{ZD}$, where d_c is the circumference of the ring and t_{ZD} the duration of the zipping-depinning process. We found a decrease of the velocity of the ZDF for decreasing ring radii. In Figure 7, the experimental data is shown. The scattering observed in the data is due to contamination and defects of the surface that pin the ZDF between the rings.

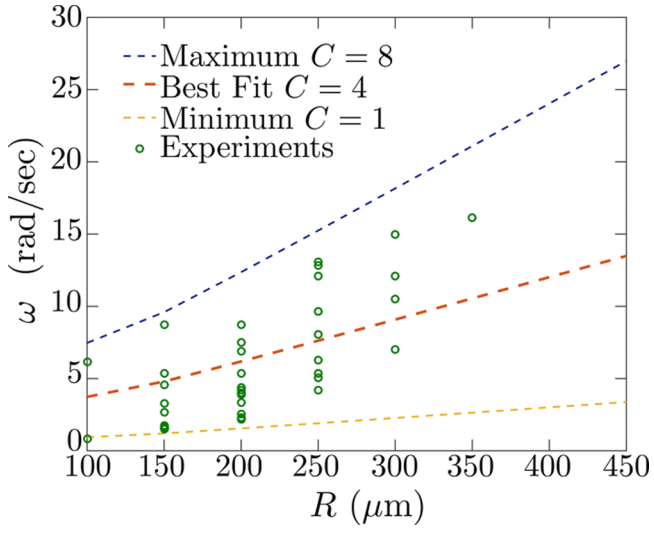

Figure 7. Experimental measurements of the angular velocity compared to the predicted values, as obtained from eq 8. A good fit is obtained for $C = 4$. The $C = 1$ and 8 values are also given for comparison.

DOI: 10.1021/acs.langmuir.8b00256
Langmuir 2018, 34, 5396−5402

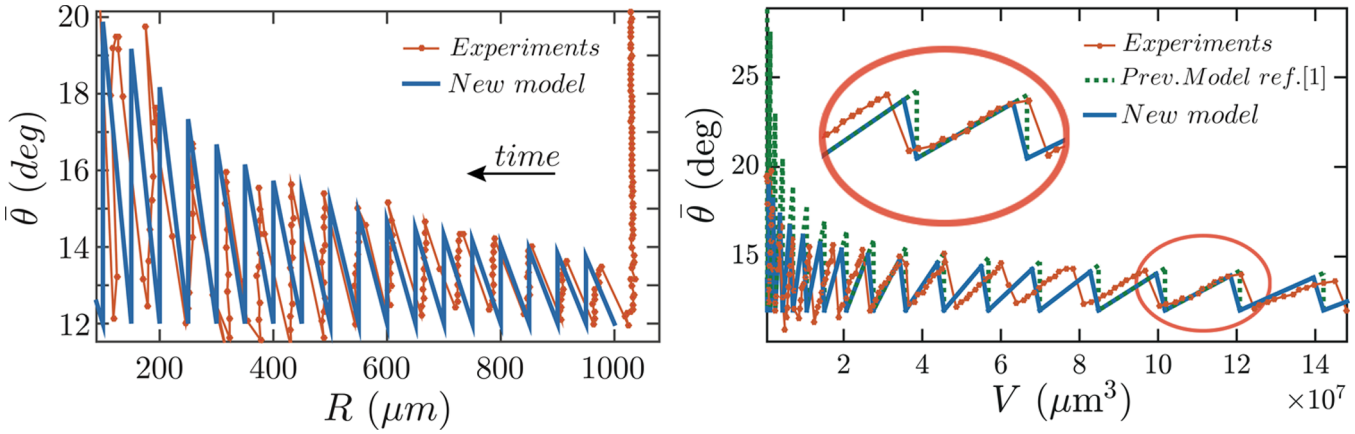

Figure 8. Experimental results for the contact angle versus the radius of the drop versus the radius R (left panel) and versus the volume V (right panel) and theoretical prediction by taking into account the volume loss during the jumps. A zoom highlights the difference between the previous model of ref 1 and the one proposed here. The new model takes into account the change in volume during each jump, in order to describe the the contact angle behavior during the whole lifetime of the droplet.

The velocity of the ZDF is governed by the dissolution rate of the droplet. To determine the velocity of the ZDF, we consider a simple model for the geometry droplet; see Figure 4c. The change of volume of the droplet can easily be approximated using the expression for the volume of a spherical cap; see Figure 4c.

By subtracting the volume integrals of the two sectors of spherical caps, we can determine the change in volume as a function of ϕ. First, we integrate over the volumes of the sectors for the two radii R_1 and R_2 as

$$V_i = \int_0^{\phi} \int_{R_i-h}^{\sqrt{R_i^2-r_i^2}} \int_0^{\sqrt{2R_i-h^2}} r \, d\phi \, dz \, dr = \phi\left(\frac{1}{2}h^2R_i - \frac{1}{6}h^3\right) =: \phi\mathcal{V}_i(R_i, h) \tag{3}$$

Therefore, the volume difference can be written as

$$V_{ZD} = V_1 - V_2 = \phi(\mathcal{V}(R_1, h) - \mathcal{V}(R_2, h)) =: \phi\Delta\mathcal{V}(R_1, R_2, h) \tag{4}$$

R_1, R_2, and h are fixed for each pair of rings, which means that the change in volume is proportional to the angle ϕ with a constant factor $\Delta\mathcal{V} = \Delta\mathcal{V}(R_1, R_2, h)$. We can write the time variation dependence of the volume associated with the ZD as follows

$$\frac{dV_{ZD}}{dt} = \Delta\mathcal{V}\frac{d\phi}{dt} = \Delta\mathcal{V}\omega \tag{5}$$

The dissolution rate is dominated by the diffusion driven mass transfer through the surroundings, as studied before by several other authors.[39,46−48] In this work, we calculate the diffusive dissolution of sessile drops, as proposed by Popov,[46] using the following expression

$$\frac{dR}{dt} = -\frac{D\Delta c}{2\rho_d R}f(\bar{\theta})\left[\frac{2}{2 - 3\cos\bar{\theta} + \cos^3\bar{\theta}}\right]^{1/3}\sin\bar{\theta} \tag{6}$$

where[46]

$$f(\bar{\theta}) = \frac{\sin\bar{\theta}}{1+\cos\bar{\theta}} + 4\int_0^{\infty}\frac{1+\cosh(2\bar{\theta}\epsilon)}{\sinh(2\pi\epsilon)}\tanh[(\pi-\bar{\theta})\epsilon]d\epsilon \tag{7}$$

is the geometrical shape factor used to model the effect of the impenetrable substrate and $\bar{\theta}$ is the macroscopic contact angle with respect to the flat substrate.

Thus, by calculating the dissolution rate dV/dt of a droplet (eq 6) and calculating $\Delta\mathcal{V}$ from the known geometries, as proposed in eq 4, we can determine the angular velocity ω from eq 5. The predicted and experimental values are shown in Figure 7. We can see that the experimentally determined velocity is always higher than the theoretically predicted velocity. This underestimation can be due to a considerable enhancement of the dissolution rate that can be expected due to the curved geometry during the zipping-depinning process,[49] which has been ignored in our calculations. Additionally, it can be influenced by the underestimation of the volume of our simple geometrical model. To counteract this effect, in Figure 6, we have introduced a fitting parameter C, which is defined as

$$\omega = C\frac{1}{\bar{\mathcal{V}}}\frac{dV_{ZD}}{dt} \tag{8}$$

to account for an increase of the effective dissolution rate. We assume that the scatter of the experimental data is due to imperfections of the substrate, showing occasional intermediate pinning points during the zipping-depinning process.

To improve the predictions, we calculate the mass loss during the transition from ring to ring using the expressions above. We compute the duration of the zipping-depinning process and evaluate the mass loss during this time to calculate the new angle $\bar{\theta}_2$. In Figure 8, we display the results of the new calculations along with the experimental results, showing an improved agreement with the data during the whole dissolution time of the droplet.

CONCLUSIONS

In summary, we have studied the dissolution of sessile microdroplets on substrates patterned with concentric geometrical grooves. We report a novel zipping-depinning mode that occurs at the late stage of the dissolution of a droplet located on concentric ring patterns. The zipping-depinning

DOI: 10.1021/acs.langmuir.8b00256
Langmuir 2018, 34, 5396−5402

takes place at a time scale one order of magnitude slower than that in the stick-jump mode. When the transition from the jumping to the zipping-depinning mode exactly occurs is still an open question. In particular, one could wonder whether it is a qualitative transition between two fundamentally different modes or whether the jumping mode is reminiscent of zipping-depinning, only occurring faster due to the change in the relative scale of the grooves with respect to the droplet size. Resolving this subject would require high-speed imaging during the experiments, which goes beyond the scope of this article. The study and understanding of the zipping-depinning mode allows for the improvement of the existing techniques to predict the contact angle hysteresis due to the underlying pattern. We have also demonstrated that the mode is controlled by the evaporative mass loss during the jumps. The dynamics of the contact line is directly related to the volume change and restricted by the geometry imposed by the pinning at the concentric rings. With our model, we can calculate the contact angles of the drop for the entire duration of the dissolution by taking into account the volume change during the zipping-depinning mode.

APPENDIX

The microfabrication process for the samples is described in ref 42 and is displayed in Figure 9. To form the micropatterned

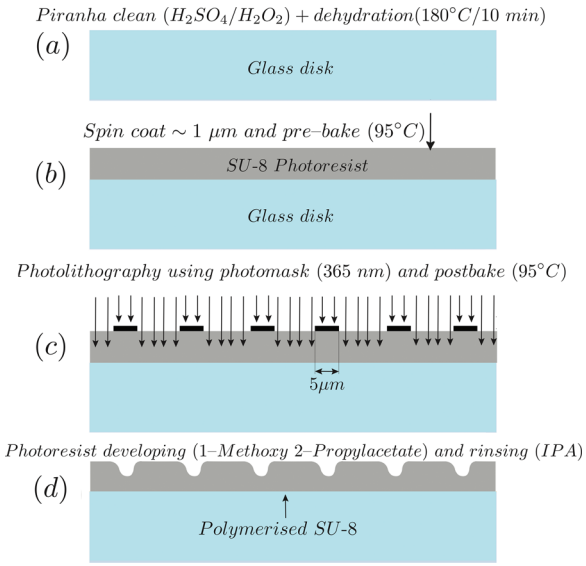

Figure 9. (a–d) Scheme of the photolithography preparation process of the substrates with concentric rings using the photoresist SU-8 as a patterned substrate prepared on top of confocal microscopy glass covers.

concentric ring samples for the experiments, two different kinds of substrates, commercial Silicon wafers (Siltronix, France) and glass disks (Thermo Scientific, Germany), are processed by photolithography, as depicted in Figure 9a–d, resulting in a smooth profile showed in Figure 9d. Figure 10 shows surface profiling obtained by scanning electron and atomic force microscopy. The techniques confirm a smooth profile of the ring. The smooth profile SU-8 defects have a height of ~560 nm and a width of ~5 m, i.e., an aspect ratio of ~10. The root mean square roughness of the SU-8 is ~3 nm. The surfaces were fabricated in a cleanroom.

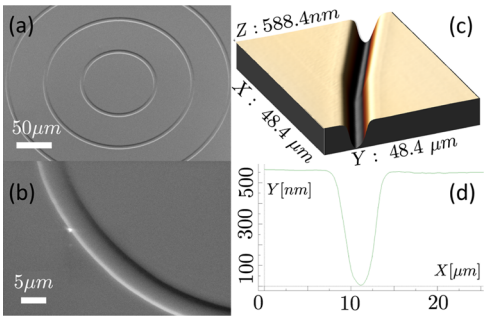

Figure 10. Scanning electron and atomic force microscopy images of the lithographic defect made using SU-8. (a) SEM of concentric circles. (b) SEM zoom. (c) Three-dimensional atomic force microscopy (AFM) image. (d) Profile obtained using AFM.

AUTHOR INFORMATION

Corresponding Authors

*E-mail: j.m.encarnacionescobar@utwente.nl (J.M.E.E.).
*E-mail: xuehua.zhang@ualberta.ca (X.Z.).
*E-mail: d.lohse@utwente.nl (D.L.).

ORCID

José M. Encarnación Escobar: 0000-0002-2527-7503
Steve Arscott: 0000-0001-9938-2683
Xuehua Zhang: 0000-0001-6093-5324
Detlef Lohse: 0000-0003-4138-2255

Notes

The authors declare no competing financial interest.

ACKNOWLEDGMENTS

We would like to acknowledge Dr. Pengyu Lv for the fruitful discussions and help as well as Javier Rodríguez Rodríguez for the inspiring conversations and invaluable help. This work was supported by the Netherlands Center for Multiscale Catalytic Energy Conversion (MCEC), an NWO Gravitation program funded by the Ministry of Education, Culture, and Science of the government of the Netherlands. X.Z. acknowledges the support from Australian Research Council (FT120100473 and LP140100594).

REFERENCES

(1) Debuisson, D.; Dufur, R.; Senez, V.; Arscott, S. *Appl. Phys. Lett.* **2011**, *99*, No. 184101.
(2) Barthlott, W.; Neinhuis, C. *Planta* **1997**, *202*, 1–8.
(3) Ohl, C. D.; Arora, M.; Dijkink, R.; Janve, V.; Lohse, D. *Appl. Phys. Lett.* **2006**, *89*, No. 074102.
(4) Gao, X.; Yan, X.; Yao, X.; Xu, L.; Zhang, K.; Zhang, J.; Yang, B.; Jiang, L. *Adv. Mater.* **2007**, *19*, 2213–2217.
(5) Zhang, Q.; He, M.; Chen, J.; Wang, J.; Song, Y.; Jiang, L. *Chem. Commun.* **2013**, *49*, 4516–4518.
(6) Zhai, L.; Berg, M. C.; Cebeci, F.; Kim, Y.; Milwid, J. M.; Rubner, M. F.; Cohen, R. E. *Nano Lett.* **2006**, *6*, 1213–1217.
(7) Cho, H. J.; Preston, D. J.; Zhu, Y.; Wang, E. N. *Nat. Rev. Mater.* **2016**, *2*, No. 16092.
(8) Patankar, N. A. *Soft Matter* **2010**, *6*, 1613–1620.
(9) Plesset, M. S.; Prosperetti, A. *Annu. Rev. Fluid Mech.* **1977**, *9*, 145–185.
(10) Marín, A. G.; Gelderblom, H.; Susarrey-Arce, A.; van Houselt, A.; Lefferts, L.; Gardeniers, J. G. E.; Lohse, D.; Snoeijer, J. H. *Proc. Natl. Acad. Sci. U.S.A.* **2012**, *109*, 16455–16458.
(11) Han, W.; Lin, Z. *Angew. Chem., Int. Ed.* **2012**, *51*, 1534–1546.
(12) Yang, H.; Wang, Y.; Song, Y.; Qiu, L.; Zhang, S.; Li, D.; Zhang, X. *Soft Matter* **2012**, *8*, 11249–11254.

DOI: 10.1021/acs.langmuir.8b00256
Langmuir 2018, 34, 5396–5402

(13) Lauga, E.; Brenner, M. *Phys. Rev. Lett.* **2004**, *93*, No. 238301.
(14) Dupuis, A.; Léopoldès, J.; Bucknall, D. G.; Yeomans, J. M. *Appl. Phys. Lett.* **2005**, *87*, No. 024103.
(15) Whitesides, G. M.; Grzybowski, B. *Science* **2002**, *295*, 2418−2421.
(16) Hannon, J. B.; Kodambaka, S.; Ross, F.; Tromp, R. *Nature* **2006**, *440*, 69−71.
(17) Sirringhaus, H.; Kawase, T.; Friend, R. H.; Shimoda, T.; Inbasekaran, M.; Wu, W.; Woo, E. P. *Science* **2000**, 2123−2126.
(18) Fan, F.; Stebe, K. J. *Langmuir* **2004**, *20*, 3062−3067.
(19) Hsiao, A. Y.; Tung, Y.-C.; Kuo, C.-H.; Mosadegh, B.; Bedenis, R.; Pienta, K. J.; Takayama, S. *Biomed. Microdevices* **2012**, *14*, 313−323.
(20) Cassie, A. B. D.; Baxter, S. *Trans. Faraday Soc.* **1944**, *40*, 546−551.
(21) de Gennes, P. G. *Rev. Mod. Phys.* **1985**, *57*, 827−863.
(22) Marmur, A. *J. Colloid Interface Sci.* **1994**, *168*, 40−46.
(23) Quéré, D. *Annu. Rev. Mater. Res.* **2008**, *38*, 71−99.
(24) Pompe, T.; Herminghaus, S. *Phys. Rev. Lett.* **2000**, *85*, 1930−1933.
(25) Herminghaus, S. *Europhys. Lett.* **2000**, *52*, 165−170.
(26) Seemann, R.; Brinkmann, M.; Kramer, E. J.; Lange, F. F.; Lipowsky, R. *Proc. Natl. Acad. Sci. U.S.A.* **2005**, *102*, 1848−1852.
(27) Rauscher, M.; Dietrich, S. *Annu. Rev. Mater. Res.* **2008**, *38*, 143−172.
(28) Méndez-Vilas, A.; Jodar-Reyes, A. B.; Gonzalez-Martin, M. L. *Small* **2009**, *5*, 1366−1390.
(29) Dietrich, E.; Kooij, E. S.; Zhang, X.; Zandvliet, H. J. W.; Lohse, D. *Langmuir* **2015**, *31*, 4696−4703.
(30) Lohse, D.; Zhang, X. *Rev. Mod. Phys.* **2015**, *87*, 981−1035.
(31) Schönfeld, F.; Graf, K. H.; Hardt, S.; Butt, H.-J. *Int. J. Heat Mass Transfer* **2008**, *51*, 3696−3699.
(32) Debuisson, D.; Merlen, A.; Senez, V.; Arscott, S. *Langmuir* **2016**, *32*, 2679−2686.
(33) Belova, V.; Gorin, D. A.; Shchukin, D. G.; Moehwald, H. *Angew. Chem., Int. Ed.* **2010**, *49*, 7129−7133.
(34) Liu, Y.; Zhang, X. *J. Chem. Phys.* **2014**, *141*, No. 134702.
(35) Nadkarni, G. D.; Garoff, S. *Europhys. Lett.* **1992**, *20*, 523−528.
(36) de Gennes, P. G.; Brochard-Wyart, F.; Quere, D. *Capillarity and Wetting Phenomena: Drops, Bubbles, Pearls, Waves*; Springer: New York, 2004.
(37) Bonn, D.; Eggers, J.; Indekeu, J.; Meunier, J.; Rolley, E. *Rev. Mod. Phys.* **2009**, *81*, 739−805.
(38) Koishi, T.; Yasuoka, K.; Fujikawa, S.; Zeng, X. C. *ACS Nano* **2011**, *5*, 6834−6842.
(39) Lohse, D.; Zhang, X. *Phys. Rev. E* **2015**, *91*, No. 031003(R).
(40) Giacomello, A.; Schimmele, L.; Dietrich, S. *Proc. Natl. Acad. Sci. U.S.A.* **2016**, *113*, E262−E271.
(41) Li, X. Y.; Cheong, B. H.-P.; Somers, A.; Liew, O. W.; Ng, T. W. *Langmuir* **2013**, *29*, 849−855.
(42) Kalinin, Y. V.; Berejnov, V.; Thorne, R. E. *Langmuir* **2009**, *25*, 5391−5397.
(43) Debuisson, D.; Senez, V.; Arscott, S. *J. Micromech. Microeng.* **2011**, *21*, No. 065011.
(44) Debuisson, D.; Senez, V.; Arscott, S. *Appl. Phys. Lett.* **2011**, *98*, No. 184101.
(45) Deegan, R. D.; Bakajin, O.; Dupont, T. F.; Huber, G.; Nagel, S. R.; Witten, T. A. *Nature* **1997**, *389*, 827−829.
(46) Popov, Y. O. *Phys. Rev. E* **2005**, *71*, No. 036313.
(47) Stauber, J. M.; Wilson, S. K.; Duffy, B. R.; Sefiane, K. *J. Fluid Mech.* **2014**, *744*, No. R2.
(48) Zhang, X.; Wang, J.; Bao, L.; Dietrich, E.; van der Veen, R. C. A.; Peng, S.; Friend, J.; Zandvliet, H. J. W.; Yeo, L.; Lohse, D. *Soft Matter* **2015**, *11*, 1889−1900.
(49) Sáenz, P. J.; Wray, A. W.; Che, Z.; Matar, O. K.; Valluri, P.; Kim, J.; Sefiane, K. *Nat. Commun.* **2017**, *8*, No. 14783.

DOI: 10.1021/acs.langmuir.8b00256
Langmuir 2018, 34, 5396−5402